Journal of Energy Storage 52 (2022) 104795

Contents lists available at ScienceDirect

Journal of Energy Storage

journal homepage: www.elsevier.com/locate/est

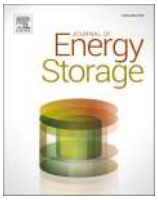

Research Papers

Bayesian optimization for effective thermal conductivity measurement of thermal energy storage: An experimental and numerical approach

Lizhong Yang [a,b], Antoni Gil [a], Pammy S.H. Leong [a], Jun Onn Khor [a], Bakytzhan Akhmetov [a], Wooi Leong Tan [c], Srithar Rajoo [d], Luisa F. Cabeza [b], Alessandro Romagnoli [e,*]

[a] Surbana Jurong – Nanyang Technological University Corporate Lab, 61 Nanyang Drive, 637355, Singapore
[b] GREiA Research Group, Universitat de Lleida, Pere de Cabrera s/n, 25001 Lleida, Spain
[c] Energy & Industrial Division, Surbana Jurong, 168 Jalan Bukit Merah, 150168, Singapore
[d] UTM-LoCARtic, Universiti Teknologi Malaysia (UTM), Johor, Malaysia
[e] School of Mechanical and Aerospace Engineering, Nanyang Technological University, 50 Nanyang Avenue, 639798, Singapore

ARTICLE INFO

Keywords:
Thermal energy storage (TES)
Phase change material (PCM)
Machine learning
Bayesian optimization
Effective thermal conductivity
Thermal contact resistance

ABSTRACT

The increasing demand for cooling and refrigeration poses an urgent need in designing efficient and low-cost thermal energy storage systems for future energy systems. While multiple effects may affect the heat transfer behaviors during thermal energy storage, these effects can be lumped into one parameter, the effective thermal conductivity. Effective thermal conductivity provides a simple and reliable solution for accurate numerical simulations in designing a thermal energy storage system. In this study, a novel experimental, numerical and Bayesian optimization-based method is developed and validated that allows for fast and accurate measurement of the effective thermal conductivities over a wide temperature range. The method can also be applied to other bulky and heterogeneous structures that cannot be considered as continuous media. An experimental setup and a 3D numerical model were developed for the plate-type thermal energy storage. After a thorough algorithm comparison, Bayesian optimization using Gaussian process was selected to search for the effective thermal conductivities with high accuracy (root mean square error < 2 K and R-squared between 0.975 and 0.992). The effective thermal conductivities measured using deionized water as the phase change material were validated by a COMSOL simulation. With the accurate effective thermal conductivity results, we revealed that neglecting the effective thermal conductivity for the solid phase while still using conduction models will lead to significant errors in the simulation. A duo arch-shaped graphite sheet-based macrofiller is designed and inserted into the plate-type thermal energy storage, which increased the effective thermal conductivities by around 20% and suppressed the subcooling effect.

1. Introduction

The demand for heating and cooling currently accounts for around 50% of global final energy consumption and more than 40% of energy-related CO2 emissions [1]. These numbers are still growing rapidly as a result of economic growth, urbanization, and climate change [1–3]. In this context, thermal energy storage (TES) is playing an increasingly important role in the energy industry by decoupling the heat and cold consumptions from their productions, which is subjected to the spatial and temporal availability of the energy supply, especially from the renewable sources [4]. The worldwide TES capacity is expected to triple in the next decade and reach over 800 GWh in 2030 [4,5], posing an urgent need in designing efficient and affordable TES units with the most suitable heat transfer enhancement techniques for future energy systems.

Numerical simulation is one of the first and most vital steps in designing a TES unit [2,6]. However, the highly complex conjugate heat transfer by both conduction and convection during the TES operation adds to the complexity of the numerical models and impedes accuracy. The process becomes even more complex if heat transfer enhancement techniques are applied. Taking latent heat TES using phase change materials (PCMs) as an example, several mechanisms have significant impacts on the heat transfer and the overall performance of a TES unit: natural convection [7–9] and free movements of solid PCM in unconstrained melting [8,10,11] can enhance the heat transfer, whereas

* Corresponding author.
E-mail address: a.romagnoli@ntu.edu.sg (A. Romagnoli).

https://doi.org/10.1016/j.est.2022.104795
Received 8 March 2022; Accepted 2 May 2022
Available online 11 May 2022

Nomenclature

CFD	Computational Fluid Dynamics
DI	Deionized
DSC	Differential Scanning Calorimetry
EI	Negative expected improvement
HTF	Heat Transfer Fluid
LCB	Lower confidence bound
PCM	Phase Change Material
PI	Negative probability of improvement
RTD	Resistance temperature detector
TES	Thermal Energy Storage

Subscripts

exp.	experimental
filler	Filler
k	Number of the boundary conditions
l	Liquid
m	Number of the initial conditions
mel	Melting
n	Number of the measuring points
PC	Phase change
s	Solid
sol	Solidification
w	Wall

Symbols

c_p	Specific heat capacity [J kg^{-1} K^{-1}]
d	Depth or distance [m]
h	Height [m]
k	Thermal conductivity [W m^{-1} K^{-1}]
L	Latent heat of fusion [J kg^{-1}]
LF	Liquid fraction [−]
MSE	Mean squared error [K^2]
N	Total number of samples [−]
q	Heat flow [W m^{-2}]
R	Thermal resistance [m^2 K W^{-1}]
$RMSE$	Rooted mean squared error [K]
T	Temperature [K]
t	Time [s]
w	Width [m]

Greek symbols

ΔT_{PC}	Phase transition range [K]
δ	Thickness [m]
Φ	Macrofiller volumetric fraction [−]
ρ	Density [kg m^{-3}]

subcooling [12,13] and thermal contact resistance [14–16] deteriorate the TES unit's performance. Considering these mechanisms in a numerical model will make the simulation process considerably complicated. As a result, despite their influence on the accuracy, most studies ignore at least one of these effects [14,17–19].

A simple yet accurate method for TES simulation, on the other hand, is widely adopted to avoid these issues. Incorporating the effects of all the complex heat transfer mechanisms into one parameter: the *effective thermal conductivity*, or k_{eff}, can simplify the heat transfer of a TES unit to a heat conduction process [20,21]. Henceforth, the complexity of the simulation can be significantly reduced while still providing reliable approximations of the TES performance for the system design [21,22].

Moreover, k_{eff} is essential to evaluating TES systems using macrofillers to enhance heat transfer. Due to the generally low thermal conductivity of the TES materials, heat transfer enhancement techniques are commonly used to improve the performance of the TES units. These techniques mainly include 1) adding *microfillers* (such as nucleating and thickening agents [2,23]) to the TES materials; and 2) inserting *macrofillers* (such as metal foams [24], metal plates [25], metal pins [26], graphite matrix [7,27], metal wool [28], carbon fiber cloths and brushes [29]) into the TES material enclosures. Compared to microfillers, inserting macrofillers, or *fixed high-conductivity inserts* [30], provide several advantages such as no particle precipitation problem, ease of manufacturing, and can be engineered to reduce the thermal contact resistance. However, the TES material domain will also become heterogeneous, as it contains both the TES material and the macrofiller. The thermal conductivity of such a domain cannot be directly measured by material-level experimental instruments, such as modulated differential scanning calorimetry (mDSC) [31] and laser flash [32]; or methods for homogeneous and isotropic medium, such as hot-wire method [33,34] and probe method [32]. As a result, a k_{eff} representing the overall heat conduction properties of the TES unit with macrofillers can be used to evaluate its performance.

Previous research mentioned two types of methods to determine the k_{eff} of a TES unit with bulky and heterogeneous structures: the direct and indirect methods.

Direct methods compute the k_{eff} directly from measured variables using specific equations. As described by Yüksel [32] and Palacios et al. [35], direct methods can be either steady-state or transient. For example, the steady-state heat flow meter method guards the material sample between a hot plate and a cold plate to generate one-directional heat conduction. A heat flux sensor is used to detect the heat flow, and adequate insulation is needed to avoid heat leakage. The k_{eff} can then be calculated from Fourier's Law. This method is widely applied to the measurement of k_{eff} values, including PCMs with two distinctive phases [36] and copper foam fillers [30]. On the other hand, Prieto et al. [37] used the transient plane source hot-disk technique to measure the k_{eff} of metal wool-resin compounds. In this method, the k_{eff} is calculated from an equation involving the sensor power input, sensor geometry, time, and temperature increase. In general, direct methods are simple in terms of the calculation of the k_{eff} values and can produce reliable results as long as the heat flux sensors can be precisely calibrated, or the electric heat input can be accurately quantified. However, direct methods have some drawbacks. Firstly, they cannot evaluate the overall behavior of the TES materials during a complete charging/discharging process within one measurement. Steady-state can be difficult to reach and maintain if extra heat or cold is supplied during the measurement while the phase change is ongoing, and transient methods can only measure the k_{eff} of an instant. To obtain the relationship between the steady-state k_{eff} and the mean temperature, Yang et al. [36] had to assume a quasi-steady-state phase change and conduct a series of measurements at various different temperatures. Secondly, direct methods require a well-controlled environment to minimize the effect of heat leakage on the measured heat/cold flow, which becomes challenging if the measuring temperature deviates far from the ambient. To minimize the heat leakage, Feng et al.'s [30] experiments (using water as the PCM) were carried out in the cold winter with a room temperature of −12 °C. Last but not least, thermal contact resistance between the samples and the sensors affects the measuring accuracy. Pressure is usually applied to decrease but not eliminate the thermal contact resistance, which may affect the reliability of the measured k_{eff} results.

On the contrary, indirect methods can cover the whole charging/discharging process, function over a considerably wider temperature range, and incorporate the effect of thermal contact resistance into the k_{eff}. This type of method uses computational fluid dynamics (CFD) models to generate numerical simulation results, which will be

compared with the experimental results. Through the comparison, the k_{eff} values that make the numerical data fit the best with the experimental data will be output as the measuring results. Facilities like thermal baths, which are widely used in indirect methods, are easier for heat leakage control. Hence, indirect methods can provide a more extensive temperature range. The experiments can be carried out at temperature conditions similar to those in which the TES will be used in real applications. Using indirect methods, Bédécarrats et al. [22], Amin et al. [38], Tay et al. [39], and Aziz et al. [26] developed complex CFD models to obtain the k_{eff} values for liquid PCMs encapsulated in spheres and shell-and-tube TES units. However, compared to direct methods, the existing indirect methods are either less accurate or more time-consuming because considerable rounds of CFD iterations are required to determine the most appropriate k_{eff} value. Searching for the k_{eff} value manually is inefficient, can fall into a local optimum, and can only offer low-precision results. The difficulty of manual searching also increases exponentially if more than one k_{eff} values – for example, the effective thermal conductivities for both liquid and solid phases of the PCMs ($k_{eff,\,l}$ and $k_{eff,\,s}$) – are required. As can be seen in the studies of Borri et al. [13], Bédécarrats et al. [22], and Aziz et al. [26], adopting the concept of effective thermal conductivity only for the liquid phase, while neglecting the effects of thermal contact resistance and subcooling to the solid phase, led to a faster increase and decrease of the solid temperature during the melting and solidification process. In order to obtain the most accurate values for both $k_{eff,\,l}$ and $k_{eff,\,s}$, Waser et al. [40] developed an fast-computing 1D CFD model and applied the grid search method – scanning a wide range of possible combinations by uniform sampling of $k_{eff,\,l}$ and $k_{eff,\,s}$ values – to ensure the global optimum is reached. The accuracy of such a method is limited by the sampling density and the quality of the CFD model, but high sampling density and sophisticated CFD models consume significantly more computing time. Therefore, despite of the various advantages over the direct methods, the application of indirect methods is constrained by the inefficient and inaccurate k_{eff} searching process.

To overcome the shortcomings of the existing methods, a novel experimental, numerical, and Bayesian optimization-based indirect method that is accurate and fast with simple experimental facilities is presented in this study. Compared to existing indirect methods, a machine learning-based Bayesian Optimization algorithm is employed to quickly and accurately search for the most accurate values for more than one k_{eff} value simultaneously, including the k_{eff} of solid and liquid during both melting and solidification processes ($k_{eff,\,l,\,mel}$, $k_{eff,\,l,\,sol}$, $k_{eff,\,s,\,mel}$, and $k_{eff,\,s,\,sol}$). Due to the high efficiency of the algorithm, much fewer rounds of CFD iterations are needed to achieve an adequate level of accuracy. Therefore, more sophisticated CFD models, such as 2D and 3D models, or models with complex geometries, can be employed to generate more accurate simulation results. Moreover, this method is not only suitable for the TES systems but also for the other bulky and heterogeneous constructions. In this research, a 3D numerical model was developed to accurately simulate the behavior of a test cell designed for plate-type TES k_{eff} measurement. The 3D model also allows for comparing the CFD and experimental temperature profiles of more than one measuring point at various locations in the PCM domain, further increasing the accuracy of the k_{eff} measurements. The obtained k_{eff} results are discussed and validated by commercial software against the experimental data. In the last part of the paper, the method is demonstrated by measuring the k_{eff} values of TES with a novel graphite-based macrofiller design. The inserted macrofiller increased the k_{eff} by around 20% and eliminated the subcooling.

The novelties of this research are:

1) proposed a novel experimental, numerical, and Bayesian optimization-based method that enabled fast and accurate measurement of the k_{eff} values of bulky and heterogenous materials over a wide temperature range during the entire operation process;
2) accurately obtained four k_{eff} values for both liquid and solid phases during melting and solidification processes simultaneously for PCMs using the highly efficient searching algorithm;
3) provided new insights into the water used as a PCM and pointed out that neglecting the effects of thermal contact resistance and air bubble formation may lead to an overestimation of the solidification and melting speed;
4) demonstrated the usage of this method in measuring the heat transfer enhancement performance of a new macrofiller design.

2. Methodology

As illustrated in Fig. 1, the numerical and machine learning-based method proposed in this study contains three interactive parts:

a) An experimental setup that mimics a targeted TES unit's operation. The TES material sample is contained in a test cell. The temperature profiles $\boldsymbol{T}_{exp}(t)$ of more than one measuring point (from 1 to n) inside the test cell are measured and recorded in the data logger.

$$\boldsymbol{T}_{exp}(t) = \left[T_{exp,1}(t) \;\cdots\; T_{exp,n}(t)\right] \tag{1}$$

The initial and boundary conditions ($\boldsymbol{T}_{IC}$ and $\boldsymbol{T}_{BC}(t)$), such as the initial TES material temperature and wall temperatures, are also measured and recorded to be input to the CFD model.

$$\boldsymbol{T}_{IC} = [T_{IC,1} \quad \cdots \quad T_{IC,m}] \tag{2}$$

$$\boldsymbol{T}_{BC}(t) = [T_{BC,1}(t) \quad \cdots \quad T_{BC,k}(t)] \tag{3}$$

b) A CFD model to simulate the operation of the TES. With the $\boldsymbol{T}_{IC}$ and $\boldsymbol{T}_{BC}(t)$ from the measuring experiment, the CFD model generates the local temperature profiles of the measuring points based on the effective thermal conductivity input from the k_{eff} updating model.

$$\boldsymbol{T}_{CFD}\left(k_{eff}, t\right) = [T_{CFD,1}(t) \quad \cdots \quad T_{CFD,n}(t)] \tag{4}$$

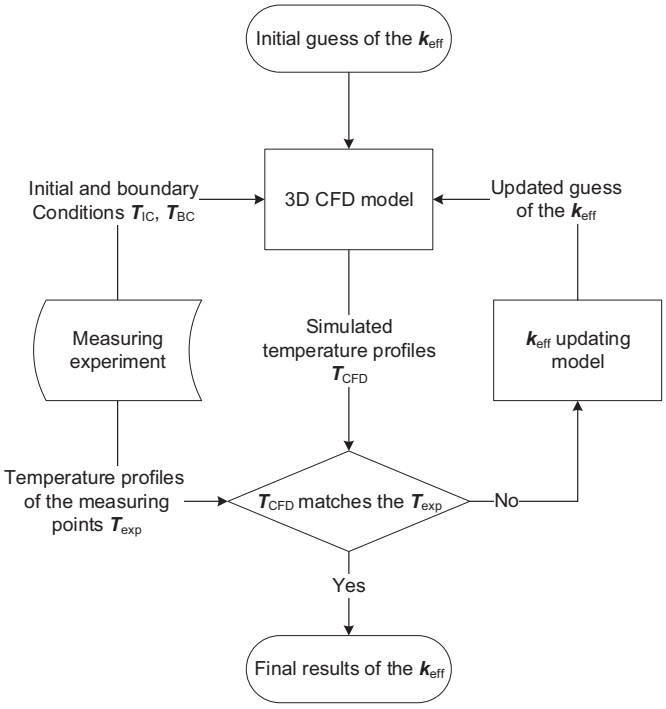

Fig. 1. The working principle of the numerical and machine learning-based method to measure the effective thermal conductivity.

c) An optimization algorithm-based k_{eff} updating model to look for the most accurate k_{eff} values. The model generates the guessed k_{eff} values for each iteration until the final $\boldsymbol{k}_{eff}$ is found that creates the best fit between $\boldsymbol{T}_{CFD}(k_{eff}, t)$ and $\boldsymbol{T}_{exp}(t)$. For sensible TES materials and other materials that do not go through phase transitions during the operation, only one k_{eff} covering the operation temperature range is needed:

$$\boldsymbol{k}_{eff} = [k_{eff}] \tag{5}$$

for PCMs, the k_{eff} values of both solidification and melting processes will be generated:

$$\boldsymbol{k}_{eff,sol} = [k_{eff,l,sol} \quad k_{eff,s,sol}] \tag{6}$$

$$\boldsymbol{k}_{eff,mel} = [k_{eff,l,mel} \quad k_{eff,s,mel}] \tag{7}$$

Details of the three parts implemented in this study are provided as follows.

2.1. Experimental setup

The experimental setup should provide accurate measurement of the temperature profiles during the TES operation. To demonstrate the method, this study used a simple setup for the design of the macro-filler for plate-type TES using PCMs. The setup comprises of two parts: a k_{eff} test cell containing the TES material and macrofiller (Fig. 2a and b), and a thermal bath that holds the test cell (Fig. 2c and d).

To ensure the results measured can be directly used in the TES design, the k_{eff} test cell should guarantee the effects of natural convection, solid movements, thermal contact resistance, and subcooling are at

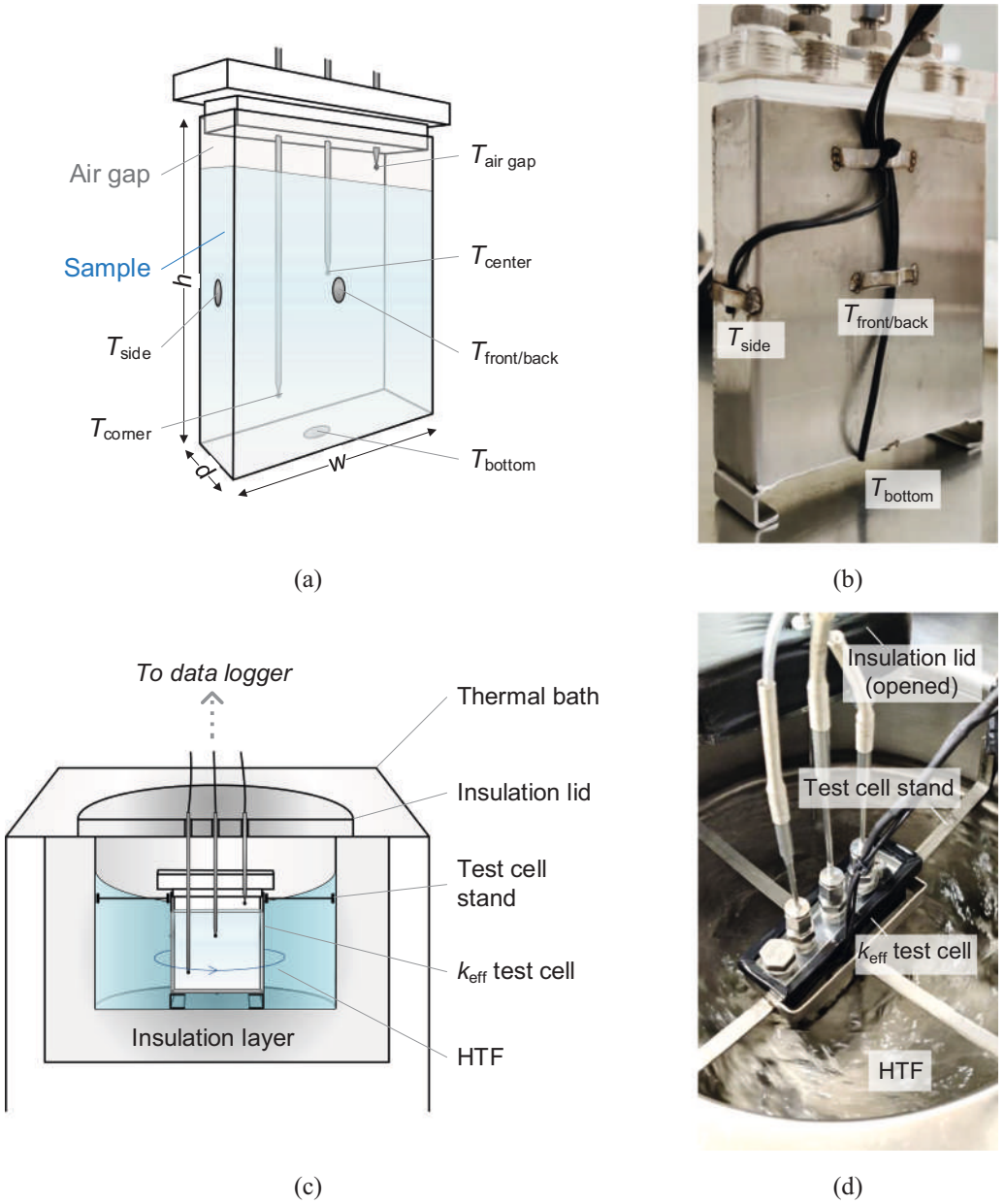

Fig. 2. Schematics and photographs of the test cell setup. (a) and (b): the k_{eff} test cell; (c) and (d) the test cell inserted into the chamber of the thermal bath. The RTDs are inserted through dedicated opening on the insulation lid, which is used to maintain the temperature inside the thermal bath chamber. The level of the HTF is kept above the level of the sample in the test cell to ensure isothermal temperature boundary conditions.

the same scale as the real-sized TES unit. As illustrated in Fig. 3, the size of the test cell was selected to be the smallest repeating structure of a macro-scale TES unit in real applications. The test cell was made with the same enclosure material and exposed to the same cooling and heating rate since the cooling rate affects the degree of subcooling [17]. In this study, the thermal bath offered controllable uniform temperature boundary conditions to the test cell by circulating the heat transfer fluid (HTF) at a high speed. 3M™ Novec™ 7100 was chosen to be the HTF due to its low viscosity compared to other HTFs at low temperatures (around 1 $mm^2\ s^{-1}$ at −20 °C).

As illustrated in Fig. 2a, six resistance temperature detectors (RTDs, Omega™ PT-100 with the maximum deviation of less than ±0.40 °C in the experimental range) were attached to the walls or inserted into the test cell to measure the boundary conditions (T_{bottom}, $T_{front/back}$ and T_{side}), the TES material temperatures (T_{center} and T_{corner}), and the air gap temperature ($T_{air\ gap}$). The shielded RTDs (T_{center}, T_{corner}, and $T_{air\ gap}$) were inserted through dedicated grooves in the insulation lid that covers the bath chamber (Fig. 2c). The insulation lid minimizes the interaction between the bath and the ambient environment and fixes the positions of the test cell RTDs together with the test cell stand.

Parameters of the test cell and thermal bath are listed in Table 1. The setup was assembled and the tests were carried out at the Thermal Energy Systems Lab at Nanyang Technological University (TESLAB@NTU) [41].

2.2. 3D CFD model

A heat conduction-based 3D finite volume CFD model was developed. Compared to 1D or 2D models used in previous studies with in-house developed codes, the 3D model is more accurate and not constrained to specific geometries of the TES units.

The key assumptions of the CFD model are listed below:

1. Both solidification and melting start from a uniform temperature distribution within the test cell. $T_{air\ gap}(t)$ is used to indicate the uniform temperature distribution is reached if it is the same as $T_{center}(t)$ and $T_{corner}(t)$.
2. Temperature boundary conditions for the bottom surface, the front and back surfaces, and the two side surfaces are measured by $T_{bottom}(t)$, $T_{front/back}(t)$ and $T_{side}(t)$, respectively. The top surface is assumed to be adiabatic since the thermal conductivity of air is significantly smaller than most solid or liquid TES materials [2]. From the experimentally validated simulation of Calvet et al. [19] for a sphere filled with water as the PCM, no noticeable temperature difference is seen above and beneath the PCM-air gap interface, indicating the heat transfer between the air gap and the PCM can be neglected.
3. The influence of the temperature sensors on the heat transfer inside and outside the test cell is neglected. Thermal contact resistance between the surface temperature sensors and the stainless steel surfaces is also neglected since they are closely attached to the test cell walls with welded clips.
4. The volume change of the PCM is neglected during the phase transition.

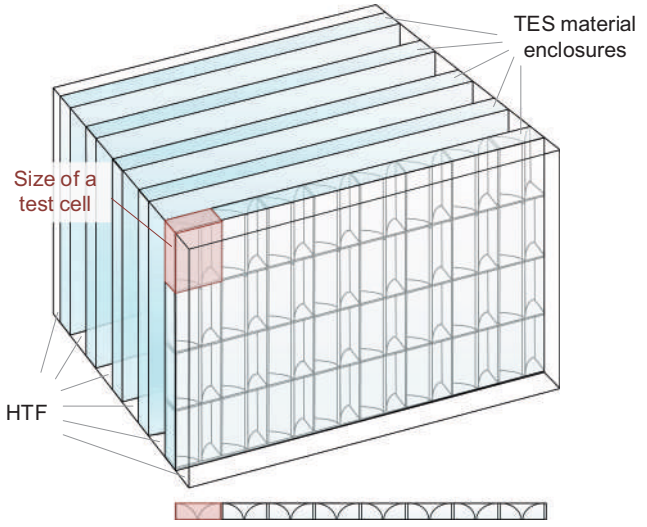

Fig. 3. Size of a k_{eff} test cell (shown in pink color) for a plate-type TES unit with the duo arch-shaped macrofillers. The size of the test cell is selected to be the smallest repeating structure of the macro-scale TES unit in real applications. (For interpretation of the references to color in this figure legend, the reader is referred to the web version of this article.)

Table 1
Specifications of the experimental setup.

Variables/items	Values/names
Test cell	
Width, w	100.4 [mm]
Height, h	110.0 [mm]
Depth, d	25.0 [mm]
Test cell material	Stainless Steel 304
Wall thickness, δ	1.5 [mm]
Wall thermal conductivity, k_w	14.0 [$W\ m^{-1}\ K^{-1}$]
Temperature sensor	Omega™ PT 100 (< ± 0.40 °C)
Thermal bath	
Heat transfer fluid	3M™ Novec™ 7100
Temperature range	−120 °C to 30 °C
Chamber material	Stainless Steel 304
Chamber diameter	210 [mm]
Chamber depth	250 [mm]

By considering only heat conduction, the energy conservation of the heat transfer is

$$\left(\Phi\rho_{filler}c_{p,filler}+(1-\Phi)\rho_{PCM}c_{p,PCM}\right)\frac{\partial T(t)}{\partial t} = k_{eff}\left(\frac{\partial^2 T(t)}{\partial x^2}+\frac{\partial^2 T(t)}{\partial y^2}+\frac{\partial^2 T(t)}{\partial z^2}\right) \quad (8)$$

where Φ is the ratio of the macrofiller volume V_{filler} in the TES material structure $V_{PCM} + V_{filler}$,

$$\Phi = \frac{V_{filler}}{V_{PCM}+V_{filler}} \quad (9)$$

ρ_{filler} and $c_{p,\ filler}$ are the density and specific heat capacity of the macrofiller material, ρ_{PCM} is the density of the PCM given by

$$\rho_{PCM} = LF\rho_{PCM,l}+(1-LF)\rho_{PCM,s} \quad (10)$$

where $\rho_{PCM,\ l}$ and $\rho_{PCM,\ s}$ are the densities of the PCM in liquid and solid phases. LF is the liquid fraction defined by

$$LF = \begin{cases} 1, & \text{when } T \geq T_{PC}+\frac{1}{2}\Delta T_{PC} \\ \dfrac{T-T_{PC}+\frac{1}{2}\Delta T_{PC}}{\Delta T_{PC}}, & \text{when } T_{PC}-\frac{1}{2}\Delta T_{PC} < T < T_{PC}+\frac{1}{2}\Delta T_{PC} \\ 0, & \text{when } T \leq T_{PC}-\frac{1}{2}\Delta T_{PC} \end{cases} \quad (11)$$

T_{PC} is the phase change temperature, and ΔT_{PC} is an assumed temperature range where the phase change takes place. Similarly, the effective thermal conductivity k_{eff} is calculated as

$$k_{eff} = LFk_{eff,l}+(1-LF)k_{eff,s} \quad (12)$$

The specific heat capacity of the PCM, $c_{p,\ PCM}$, is defined as

$$c_{p,PCM} = \begin{cases} c_{p,PCM,l}, & \text{when } T \geq T_{PC} + \frac{1}{2}\Delta T_{PC} \\ \frac{L}{\Delta T_{PC}} + LFc_{p,PCM,l} + (1-LF)c_{p,PCM,s} & \text{when } T_{PC} - \frac{1}{2}\Delta T_{PC} < T < T_{PC} + \frac{1}{2}\Delta T_{PC} \\ c_{p,PCM,s} & \text{when } T \leq T_{PC} - \frac{1}{2}\Delta T_{PC} \end{cases} \quad (13)$$

where $c_{p,\,PCM,\,l}$ and $c_{p,\,PCM,\,s}$ are the specific heat capacity of the PCM in liquid and solid phases and L is the latent heat of the PCM.

Since the effect of the thermal contact resistance between the TES material and the walls is considered as part of k_{eff}, the thermal resistance of the test cell walls, R_w, is the only thermal resistance considered in the model,

$$R_w = \frac{\delta}{k_w} \quad (14)$$

where δ and k_w are the thickness and thermal conductivity of the walls.

The 3D CFD model was developed with C++ [42] for fast computing (modified based on an open-sourced code [43]). Grid independence test showed that the 3D CFD model could generate reliable $\boldsymbol{T}_{CFD}(t)$ results with less than 10 s on a commercial laptop with an Intel Core i7-10750H central processing unit (CPU) @ 2.60GHz and a random-access memory (RAM) of 16 GB. With the temperature profiles of all measuring points $\boldsymbol{T}_{exp}(t)$ obtained from the experiments, and the other variables, Φ, ρ_{PCM}, ρ_{filler}, $c_{p,\,PCM}$, and $c_{p,\,filler}$ being either known or measurable, k_{eff} is the only unknown variable in Eq. (8). Analytically solving Eq. (8) for k_{eff} is challenging. However, the k_{eff} can be estimated with high accuracy after a certain number of iterations between the 3D CFD model and the k_{eff} updating model until a $\boldsymbol{T}_{CFD}(t)$ closest to $\boldsymbol{T}_{exp}(t)$ is found.

2.3. Optimization algorithm-based k_{eff} updating model

The goal of the k_{eff} updating model is to find out the best $\boldsymbol{k}_{eff}$ based on the previous iterations. The mean squared error (*MSE*) between the CFD and experimental temperature profiles is used as the objective function:

$$minMSE(\boldsymbol{k}_{eff}) = \frac{1}{nN}\sum_{j=1}^{N}\sum_{i=1}^{n}\left(T_{CFD,i}(\boldsymbol{k}_{eff}, j) - T_{exp,i}(j)\right)^2 \quad (15)$$

where i denotes a measuring point (T_{center} and T_{corner} in this study) and n is the total number of the measuring points; j represents a sample in $T_{CFD,\,i}(t)$ or $T_{exp,\,i}(t)$ and N is the total number of $\boldsymbol{T}_{exp,\,i}$ samples for each measuring point during the solidification or melting processes. Hence, the task of searching for the best $\boldsymbol{k}_{eff}$ is converted to an optimization problem, and an optimization algorithm can be used to look for the global optimum of Eq. (15).

The optimization algorithm should be able to conduct fast and accurate predictions from a black-box process without knowing the details inside the process except for the inputs and outputs. Therefore, in this study, we tested and compared the performance of six commonly used optimization algorithms for hyperparameter optimization, which is a well-studied black-box problem [44] similar to the $\boldsymbol{k}_{eff}$ searching problem. As a result, the widely applied Bayesian Optimization using Gaussian Process, which is a machine learning-based tool suitable for problems with objective functions that are expensive to evaluate (takes minutes or hours) [45,46], delivered the best overall performance.

In the algorithm comparison test, an artificially assumed $\boldsymbol{k}_{eff}$ and other parameters were input to the 3D CFD model to generate a hypothetical $\boldsymbol{T}'_{exp}(t)$ for the algorithm performance comparison. We compared the accuracy and execution time of four machine learning-based optimization algorithms [45]: *Bayesian optimization using Gaussian process*, *sequential optimization using extra decision trees*, *random forest*, and *gradient boosted trees*. The performance of *random search by uniform sampling* [45] and the commonly used *genetic algorithm* [47] are also employed for reference in the comparison.

The accuracies of the algorithms are expressed in terms of root mean squared errors (*RMSE*), which is defined as:

$$RMSE = \sqrt{MSE} \quad (16)$$

During the algorithm comparison test, the execution time of the genetic algorithm was significantly longer than the other algorithms (can be even ten times longer). At the same time, its results were not consistent regardless of the population sizes: increasing the number of calls will not always increase the accuracy. Therefore, only the results of

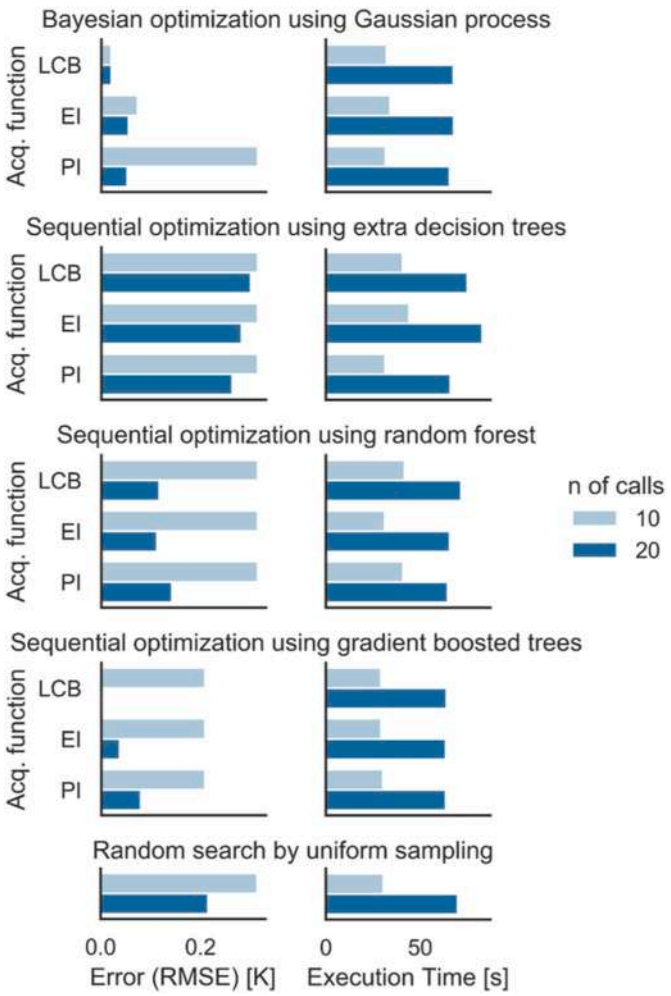

Fig. 4. Performance comparison of the algorithms for $\boldsymbol{k}_{eff}$ searching. Bayesian optimization using Gaussian process with LCB as the acquisition function delivered the best performance. (Types of acquisition functions used to compare the algorithms: LCB – lower confidence bound; EI – negative expected improvement; PI – negative probability of improvement).

the other five algorithms are summarized in Fig. 4.

During the test, we found no significant difference in the execution time for all of the algorithms except for the genetic algorithm. In terms of accuracy, Bayesian optimization using Gaussian process and lower confidence bound (LCB) as the acquisition function achieved an *RMSE* of 0.02 K after only 10 calls (or iterations between the 3D CFD model and the k_{eff} updating model). The other algorithms failed to attain this level even after 20 calls, except for sequential optimization using gradient boosted trees and LCB, which obtained an error of 0.003 K. However, its error after 10 calls is around 10 times of Bayesian optimization using Gaussian process and LCB. Hence, the latter demonstrated the best overall performance in terms of both accuracy and speed, proving itself more suitable for the $\boldsymbol{k}_{eff}$ searching task. The result is similar to the conclusion drawn by Turner et al. [44]. After analyzing the outcomes of a black-box optimization competition, they found that Bayesian optimization demonstrated decisively better performance than random search, and all of the top-performing teams in the competition used some forms of Bayesian optimization for the machine learning hyperparameter optimization tasks.

Therefore, Bayesian optimization using Gaussian process and LCB was selected as the algorithm of the k_{eff} updating model for this study. The model was developed in Python [48]. The stopping criteria of the iteration between the 3D CFD model and the k_{eff} updating model was set to be less than 0.1% of improvement in *MSE* compared to the previous call, ensuring the most accurate k_{eff} values were found.

3. Results and discussion

3.1. Testing with DI water and validation of the algorithm generated $\boldsymbol{k}_{eff}$

To validate the method's functionality, we used deionized (DI) water as the PCM for the validation tests. The measurements were carried out between 20 °C and − 20 °C with the temperature of the HTF circulating around the test cell controlled by the thermal bath.

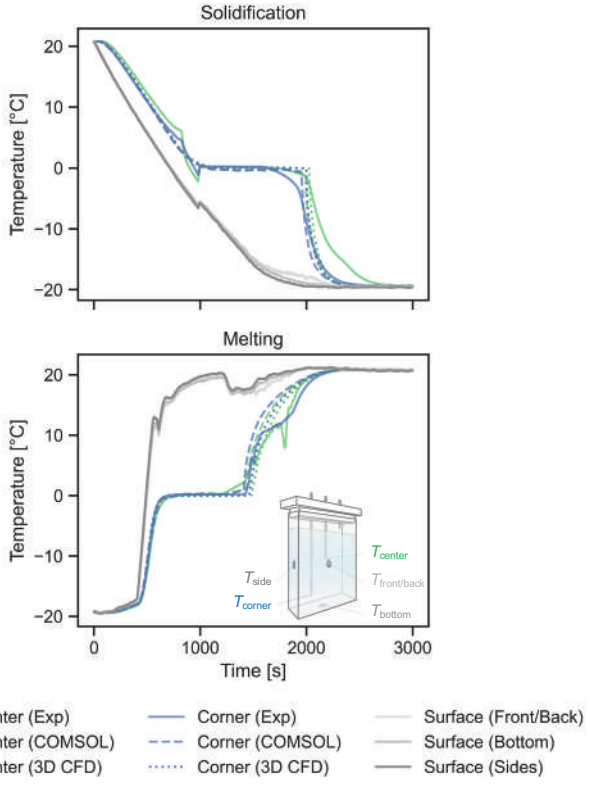

Fig. 5. Comparison of the temperature profiles from the experiment, COMSOL validation, and the best results from the 3D CFD model of DI water as the TES material.

The experimentally measured temperature profiles $\boldsymbol{T}_{exp}(t) = [\,T_{exp,center}(t) \quad T_{exp,corner}(t)\,]$ are shown in solid lines in Fig. 5. During the solidification process, T_{center} and T_{corner} shifted due to the water density change at around 4 °C, the same phenomenon as explained by Calvet et al. [19]. The subcooling degrees of the bottom and center measuring points were 1.1 and 2.2 °C, indicating that subcooling is not uniform across the whole PCM domain. During the melting process, the unmelt ice moves both horizontally and vertically due to the buoyancy within the test cell, causing the temperature profiles to fluctuate. Moreover, the average difference between the test cell surface temperatures ($T_{bottom}(t)$, $T_{front/back}(t)$, and $T_{side}(t)$) was found to be below 0.5 °C, suggesting that the temperature uniformity within the HTF was well controlled and $[\,T_{bottom}(t) \quad T_{front/back}(t) \quad T_{side}(t)\,]$ can be used as the boundary condition $\boldsymbol{T}_{BC}(t)$.

The measured initial and boundary conditions were hence fed into the 3D CFD model to generate the $\boldsymbol{T}_{CFD}(t) = [\,T_{CFD,center}(t) \quad T_{CFD,corner}(t)\,]$. Table 2 lists the properties of the DI water used in the 3D CFD model. On the other hand, the measured TES material temperatures $\boldsymbol{T}_{exp}(t)$ were input to the k_{eff} updating model for the searching of the effective thermal conductivities for solid and liquid during the solidification and melting processes: $\boldsymbol{k}_{eff,sol} = [\,k_{eff,l,sol} \quad k_{eff,s,sol}\,]$ and $\boldsymbol{k}_{eff,mel} = [\,k_{eff,l,mel} \quad k_{eff,s,mel}\,]$.

With around 10 to 15 calls, as listed in Table 3, the Bayesian optimization algorithm using Gaussian process was able to reach the stopping criteria and achieve the R^2 values of 0.983 and 0.992 for $\boldsymbol{k}_{eff,\,sol}$ and $\boldsymbol{k}_{eff,\,mel}$ respectively, significantly more efficient than manual search or grid search methods used in previous research. The *RMSE* were as low as 1.60 and 1.26 K. Considering the effects of water density shift, subcooling, and ice movements, the *RSME* could not reach the level of 0.02 K in the algorithm comparison test. The $\boldsymbol{T}_{CFD}(t)$ generated by the 3D CFD model using the $\boldsymbol{k}_{eff}$ values found are plotted in Fig. 5 in dotted lines, matching well with the $\boldsymbol{T}_{exp}(t)$ profiles.

To validate the algorithm generated $\boldsymbol{k}_{eff}$ results, a *COMSOL Multiphysics* model with the *Phase Change Material* subnode was employed. The default settings were adopted by just changing the material properties according to Table 2 and using the $\boldsymbol{k}_{eff}$ values obtained from the algorithm. Due to simulation convergence reasons, a larger ΔT_{PC} of 1.2 K was adopted in the COMSOL model compared to 0.1 K in the 3D CFD model. The temperature profiles obtained from the COMSOL simulation are plotted in Fig. 5 with dashed lines, and they matched the experimental and 3D CFD profiles quite well. Therefore, the results successfully validated the numerical and machine learning-based method, indicating that the algorithm generated $\boldsymbol{k}_{eff}$ values can be used in other CFD tools to accurately predict the TES material's performance by just considering heat conduction in the models. Therefore, this measuring method can be used for TES system design and other applications.

Moreover, the $\boldsymbol{k}_{eff}$ found in this study provided new insights into water being used as the PCM for TES in real applications.

In general, the $\boldsymbol{k}_{eff}$ values during the melting process are higher than that of the solidification process. The difference might be attributed to two factors: 1) As described by Tan [11], the constant movements of the

Table 2
Parameters of the PCM (DI water) used in the 3D CFD model and the COMSOL validation model.

Variable	Value
Volume, V_{PCM}	151.3 [mL]
Specific heat (liquid), $c_{p,\,PCM,\,l}$	4200 [J kg^{-1} K^{-1}]
Specific heat (solid), $c_{p,\,PCM,\,s}$	2000 [J kg^{-1} K^{-1}]
Density (liquid), $\rho_{PCM,\,l}$	1000 [kg m^{-3}]
Density (solid), $\rho_{PCM,\,s}$	919 [kg m^{-3}]
Phase change temperature, T_{PC}	273.15 [K]
Phase transition range, ΔT_{PC}	0.1 [K] in the 3D CFD model 1.2 [K] in the COMSOL model
Latent heat, L	334.0 [kJ kg^{-1}]

Table 3
Algorithm generated $\boldsymbol{k}_{\text{eff}}$ for DI water as the PCM.

	$k_{\text{eff, l}}$ [W m^{-1} K^{-1}]	$k_{\text{eff, s}}$ [W m^{-1} K^{-1}]	*RMSE* [K]	R^2
Solidification	1.21	1.39	1.60	0.983
Melting	1.26	1.48	1.26	0.992

Table 4
Comparison between the $k_{\text{eff, l}}$ values obtained in this study with values in various studies (the $k_{\text{eff, s}}$ values are not compared since they are not considered in these studies).

	TES material enclosure type	Liquid phase effective thermal conductivity of water, $k_{\text{eff, l}}$ [W m^{-1} K^{-1}]
Bédécarrats et al. [22]	Sphere	1.1
Amin et al. [38]	Sphere	1.1, 1.21, 1.3, 1.9 (based on the inlet HTF temperature)
Tay et al. [39]	Shell side of shell-and-tube	0.93
Borri et al. [13]	Tube	0.98
This study	Plate	1.21 (for solidification) 1.26 (for melting)

unmelt ice during the melting process due to buoyancy introduces extra natural convection, that can enhance the heat transfer and mainly increase the $k_{\text{eff, l}}$ value compared to the solidification process. 2) The subcooling effect during the solidification can delay the crystallization [22], which mainly reduces the $k_{\text{eff, s}}$ value.

For the liquid phase, the $k_{\text{eff, l, sol}}$ value of 1.21 W m^{-1} K^{-1} and $k_{\text{eff, l, mel}}$ of 1.26 W m^{-1} K^{-1} are in good agreement with the previous studies in the literature as listed in Table 4. It is worth noting that these studies did not distinguish between the $k_{\text{eff, l}}$ during the solidification and melting processes, while the machine learning-based algorithms in this study enabled such a function with higher accuracy.

For the solid phase, nonetheless, the concept of effective thermal conductivity is adopted in much fewer studies than the liquid phase. The value of $k_{\text{eff, s, sol}} = 1.39$ W m^{-1} K^{-1} and $k_{\text{eff, s, mel}} = 1.48$ W m^{-1} K^{-1} are found to be lower than the material thermal conductivity k_s values of ice (from 2.16 at 0 °C to 2.38 at −20 °C W m^{-1} K^{-1} [49–51]), similar to what has also been found in the research of Feng et al. [30] and Waser et al. [40] who also considered both $k_{\text{eff, l}}$ and $k_{\text{eff, s}}$. In Feng et al.'s study, the effective thermal conductivity of liquid water and copper foam filler $k_{\text{eff, l}}$ reached 1.95 W m^{-1} K^{-1} with a porosity of 0.98, which is more than three times the material thermal conductivity k_l (around 0.6 W m^{-1} K^{-1}); whereas the effective thermal conductivity of ice and copper foam $k_{\text{eff, s}}$ is only 2.24 W m^{-1} K^{-1}, equivalent to the material thermal conductivity value without adding the copper foam. Waser et al. tested the $k_{\text{eff, s}}$ of two commercial PCMs, SU34 and SU58. They discovered that the measured $k_{\text{eff, l}}$ value differed 5% from an analytical model, while the $k_{\text{eff, s}}$ value was only 1/3 of the analytical value.

The deviation between the measured solid phase effective thermal conductivity $k_{\text{eff, s}}$ values and the material thermal conductivity values k_s might be attributed to two factors: the 1) thermal contact resistance caused by the gaps between the solid PCM and the enclosure walls, as well as the cracks between various layers in the solid structure, and 2) the air bubbles formed during solidification.

During the solidification process, the solidified PCM may shrink due to increased density, and hence detach from the enclosure walls, causing a non-negligible thermal contact resistance. Waser et al. [40] ascribed their decrease of $k_{\text{eff, s}}$ from the therotical values to this explanation. In this study, by using the model developed by Weigand and Lipnicki [14], we calculated the width of the gaps between the ice and the test cell walls, which ranged between 1.6 and 7.0 × 10^{-5} m for different walls. Such small widths are difficult to observe while it may still exist. According to Lipnicki and Małolepszy [52], the contact layer between the cooled wall and the solidified layer has a significant impact on the solidification process. For composite PCMs, thermal contact resistance can even account for up to 50% of total thermal resistance [16]. Furthermore, various layers of ice may form during the solidification process, resulting in visible cracks between the ice frozen at different stages of solidification. Several layers of cracks were observed (as shown in the left part of Fig. 6a) in this study using a camera with a macro and fixed focal length lens.

On the other hand, the ice formed in this study is far from perfect or uniform crystal. According to Maeno [53], McClane et al. [54], Yakhno and Yakhno [55], during the solidification process, air, being the main impurity in the distilled water, may nucleate accompanying the phase transition. Due to the sudden decrease of the air dissolvability in the water during the solidification, the released air might be trapped in the ice formation and form spherical or needle-shaped bubbles. Since the experiments were conducted with an air gap on top of the test cell mimicking the air cushion in real TES installations, many air bubbles were observed in the ice formation under the camera (Fig. 6b and the right part of Fig. 6a). These air bubbles can reduce the $k_{\text{eff, s}}$. According to Huang et al. [56], the $k_{\text{eff, s}}$ of reservoir freshwater ice filled with air bubbles can be as low as around 0.6 W m^{-1} K^{-1}, significantly lower than

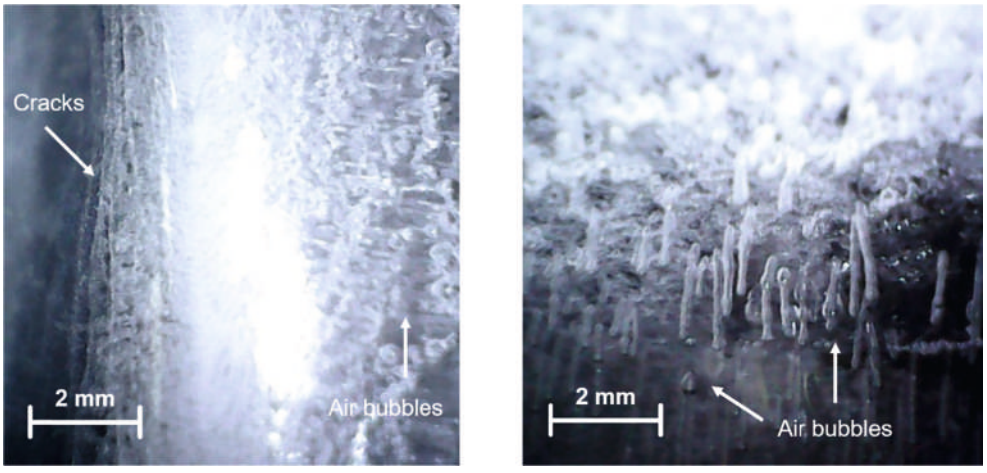

(a) (b)

Fig. 6. Possible effects that reduced the $\boldsymbol{k}_{\text{eff}}$ of ice: (a) cracks formed and air bubbles trapped in the ice during the solidification; (b) air bubble release during the melting process.

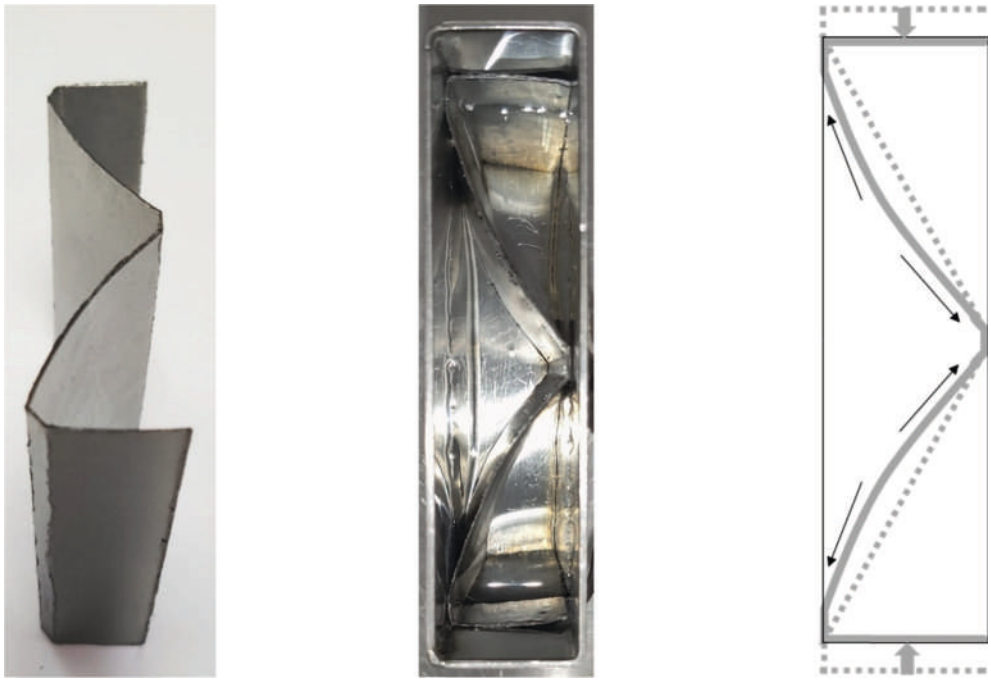

Fig. 7. The duo arch-shaped graphite sheet-based macrofiller (a) before, (b) after, being inserted into the test cell and (c) the deformation after the insertion: the dashed grey line represents the original shape of the filler, and the solid grey line presents its shape after being inserted into the test cell. The bent parts provide the supporting forces allowing for good thermal contact between the filler and the enclosure walls or the adjacent fillers as demonstrated in Fig. 3.

the material thermal conductivity k_s.

Moreover, both the thermal contact resistance [15] and the effective thermal conductivity of ice with air bubbles [56] increase when the temperature decreases. Therefore, similar to the approach adopted by Waser et al. [40], time and temperature-independent constant $k_{\text{eff, s, sol}}$ and $k_{\text{eff, s, mel}}$ values are used for this study.

3.2. Testing of a graphite sheet-based macrofiller design

To demonstrate the method for measuring the k_{eff} of heterogeneous structures, we designed a duo arch-shaped graphite sheet-based macrofiller for the plate-type TES heat transfer enhancement (Fig. 7a) and measured its k_{eff} values using the test cell (Fig. 7b). The graphite sheet-based macrofiller avoided the precipitation and complex manufacturing processes encountered in some other heat transfer enhancement techniques. Moreover, to further reduce the thermal contact resistance, the width of the filler structure is engineered to be larger than that of the PCM enclosure (Fig. 7c). After insertion, the arch-shaped parts bend and press the other parts of the filler structure against the walls using the tensile force. During the volume change of the PCM, better contact between the graphite sheet and the test cell walls may therefore be achieved. Furthermore, the design of the macrofiller is scalable. Rows and columns of the same structure can be installed in a full-sized plate-type TES unit, as illustrated in Fig. 3. The k_{eff} values measured by the test cell can directly be used for the design of a real-sized plate-type TES unit using such a filler.

Table 5
Properties of the graphite-based macrofiller used in the 3D CFD model.

Variable	Value
Purity	>99.95%
Apparent density, ρ_f	1194.1 [kg m^{-3}]
Porosity	47.2%
Specific heat, $c_{p,\,f}$	638.9 [J kg^{-1} K^{-1}]
Thickness	0.5 [mm]
Width	150.0 [mm]
Height	85.0 [mm]

A piece of graphite sheet with the dimensions of 85.0 mm (height) × 150.0 mm (width) × 0.5 mm (thickness) and the porosity of around 50% was used as the macrofiller. The properties of the graphite sheet are listed in Table 5. 150.0 mL of DI water is used as the base PCM.

As shown in solid lines in Fig. 8, the experimentally measured temperature profiles $\boldsymbol{T}_{\text{exp}}(t) = \left[\, T_{exp,\text{center}}(t) \quad T_{exp,\text{corner}}(t) \,\right]$ showed no subcooling during the solidification process. This could be because of the high porosity of the graphite material used in this study. The graphite porous microstructures might have acted as nucleating agents and suppressed the subcooling.

With around 30 calls, the best k_{eff} values could be obtained as listed in Table 6 and summarized in Fig. 9. The *RMSE* values are slightly higher than the k_{eff} results in Table 4 but still less than 2 K, and the R^2 values are close to 0.98, indicating good accuracy. The 3D CFD model-generated $\boldsymbol{T}_{\text{CFD}}(t)$ profiles based on the k_{eff} values are plotted in dotted lines in Fig. 8, which agree well with the experimental profiles.

Table 6 and Fig. 9 clearly demonstrated the increase in k_{eff} values by inserting the macrofiller into the DI water. Compared to the k_{eff} values without the macrofiller, the effective thermal conductivities rose by 17.9% on average. The difference between $k_{\text{eff, s, sol}}$ and $k_{\text{eff, s, mel}}$ values was reduced, possibly due to the suppression of subcooling significantly increased the $k_{\text{eff, s, sol}}$. The $k_{\text{eff, l, mel}}$ value increased greater than $k_{\text{eff, l, mel}}$ (24.6% and 11.8% respectively), possibly because the filler structure divided the PCM domain into three segments (as shown in Fig. 7). Hence, during the melting process, three smaller ice bulks formed and kept on moving in the test cell instead of one large piece of ice without the macrofiller. Smaller bulks melted faster due to larger heat transfer area between the unmelt ice and melt water flowing around them. Hence, the segmentation further enhanced the heat transfer by introducing extra natural convection effect during the melting process.

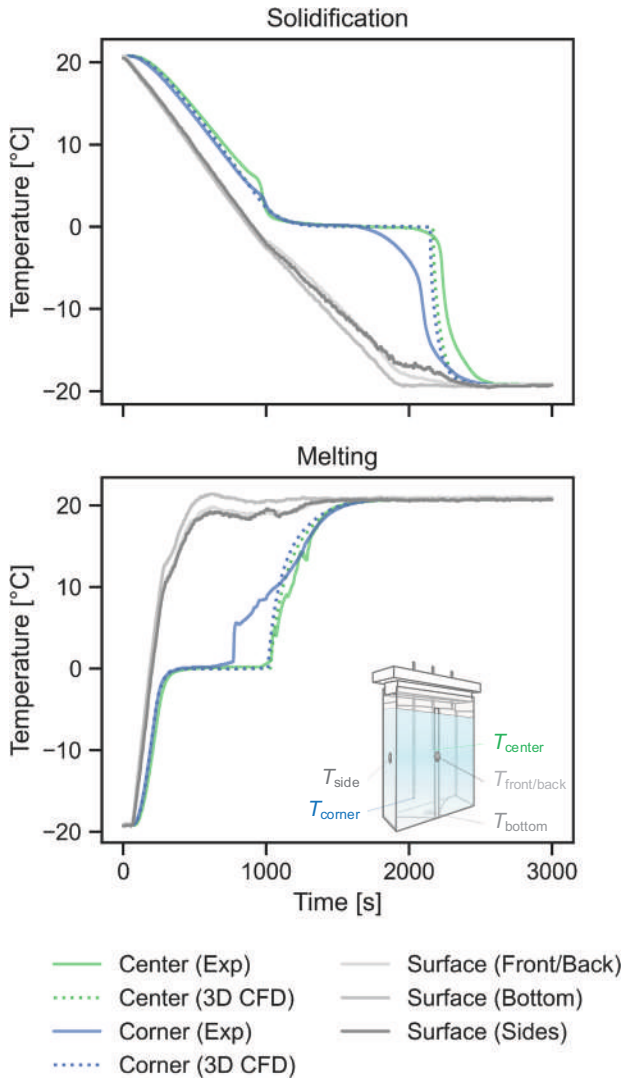

Fig. 8. Comparison of the temperature profiles from the experiment and the best results from the 3D CFD model of DI water with macrofiller.

Table 6
Algorithm generated $\boldsymbol{k}_{eff}$ after inserting the macrofiller and the improvement from DI water without the macrofiller.

	$k_{eff,\ l}$ and improvement from without the macrofiller [W m^{-1} K^{-1}] (%)	$k_{eff,\ s}$ and improvement from without the macrofiller [W m^{-1} K^{-1}] (%)	*RMSE* [K]	R^2
Solidification	1.35 (11.8%)	1.68 (21.1%)	1.98	0.975
Melting	1.57 (24.6%)	1.69 (14.1%)	1.67	0.979

Therefore, the macrofiller enhanced the heat transfer in three ways: increase the heat transfer area, suppress the subcooling, and divide the TES unit into smaller segments. The measurement results demonstrated that the macrofiller designed in this study offered an effective, affordable, easy-to-operate, and scalable (as shown in Fig. 3) solution to enhance the heat transfer of PCMs.

Moreover, compared to the phase transition time, the results also showed that k_{eff} is a more general and clearer indicator for the effectiveness of heat transfer enhancement techniques. Phase transition time varies with the boundary conditions (such as the cooling and heating rates). Precisely defining the phase transition time period is also not always easy, especially for PCMs with broad phase change temperature ranges, such as various organic PCMs. k_{eff}, on the contrary, is much less affected by the different boundary conditions and phase transition temperature ranges. Henceforth, k_{eff} allows for direct comparison between different heat transfer enhancement techniques without requiring strictly identical experimental conditions, and it is more suitable for PCMs without clear phase transition temperatures.

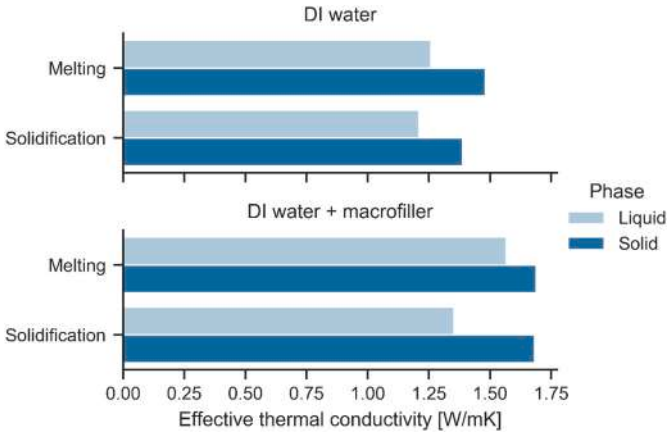

Fig. 9. Comparison of the k_{eff} values with and without the macrofiller.

4. Conclusion

In this paper, a novel numerical and machine learning optimization-based method to measure the effective thermal conductivities of thermal energy storage is developed and validated.

Traditional indirect methods for effective thermal conductivity measurement suffer from slow and inaccurate problems. This study overcomes these drawbacks by using a machine learning-based Bayesian optimization algorithm to quickly search for the most accurate effective thermal conductivity results. An experimental setup and 3D CFD model were developed to measure the effective thermal conductivities (k_{eff}) together with the algorithm based k_{eff} updating model. The measured effective thermal conductivities of using DI water as the PCM are validated by COMSOL simulation. The measured results can directly be used in designing a plate-type thermal energy storage unit in real applications. The method can also be applied to other types of TES units, as well as other bulky and heterogeneous structures that cannot be considered as continuous media. Insights were provided to the usage of water as the PCM. Thermal contact resistance and air bubble formation during the solidification may decrease the k_{eff} values. Simulations neglecting these factors will lead to an overestimation of the solidification and melting speed of solid PCMs. The method is demonstrated by measuring the k_{eff} values of a duo arch-shaped graphite sheet-based macrofiller inserted in DI water. The designed macrofiller increased the k_{eff} by around 20% and suppressed subcooling. The study also demonstrated k_{eff} as an ideal indicator for the effectiveness of heat transfer enhancement techniques.

Future studies can be carried out by applying the proposed methodology to more TES types, materials, and macrofillers, as well as quantify the effects of subcooling, unmelt PCM movements, thermal contact resistance, and air bubble formation on the effective thermal conductivities.

Declaration of competing interest

The authors declare that they have no known competing financial interests or personal relationships that could have appeared to influence the work reported in this paper.

Acknowledgment

We thank Prof. Chun Yang (School of Mechanical and Aerospace Engineering, Nanyang Technological University), Mr. Qiu Zheng, Dr. Bingjie Wu, Dr. Rahul Singh, Dr. Alessio Tafone (Surbana Jurong – Nanyang Technological University Corporate Lab), Dr. Xueqing Liu (Columbia University), Dr. Ran Zhang (Hasso Plattner Institute), and the colleagues from the TESLAB@NTU for their help in this study.

The authors would like to acknowledge the funding support from SJ-NTU Corporate Lab at Nanyang Technological University. This study is supported under the RIE2020 Industry Alignment Fund – Industry Collaboration Projects (IAF-ICP) Funding Initiative, as well as cash and in-kind contribution from Surbana Jurong Pte Ltd.

This research is partially funded by the Ministerio de Ciencia Innovación y Universidades de España (RTI2018-093849-B-C31—MCIU/AEI/FEDER, UE), and the Ministerio de Ciencia, Innovación y Universidades—Agencia Estatal de Investigación (AEI) (RED2018-102431-T). This work is partially supported by ICREA under the ICREA Academia programme. The authors at the University of Lleida would like to thank the Catalan Government for the quality accreditation given to their research group (2017 SGR 1537). GREiA is a certified agent TECNIO in the category of technology developers from the Government of Catalonia.

References

[1] IRENA, IEA and REN21 (Ed.), Renewable Energy Policies in a Time of Transition: Heating and Cooling, IRENA, OECD/IEA and REN21, 2020.
[2] L. Yang, U. Villalobos, B. Akhmetov, A. Gil, J. Onn, A. Palacios, et al., A comprehensive review on sub-zero temperature cold thermal energy storage materials, technologies, and applications: state of the art and recent developments, Appl. Energy 288 (2021), 116555, https://doi.org/10.1016/j.apenergy.2021.116555.
[3] United Nations Environment Programme. The Importance of Energy Efficiency in the Refrigeration and Heat Pump Sectors. 2018.
[4] IRENA, Innovation Outlook: Thermal Energy Storage, International Renewable Energy Agency, Abu Dhabi, 2020.
[5] IRENA, Innovation Outlook: Thermal Energy Storage, International Renewable Energy Agency, Abu Dhabi, 2020.
[6] L. Yang, U. Villalobos, B. Akhmetov, K.J. Onn, A. Gil, W.L. Tan, et al., Active TES with PCM for refrigeration applications, Encycl. Energy Stor. (2021), https://doi.org/10.1016/B978-0-12-819723-3.00029-9. Elsevier.
[7] L.F. Cabeza, H. Mehling, S. Hiebler, F. Ziegler, Heat transfer enhancement in water when used as PCM in thermal energy storage, Appl. Therm. Eng. 22 (2002) 1141–1151, https://doi.org/10.1016/S1359-4311(02)00035-2.
[8] Z. Gao, Y. Yao, H. Wu, Validation of a melting fraction-based effective thermal conductivity correlation for prediction of melting phase change inside a sphere, Int. J. Therm. Sci. 142 (2019) 247–257, https://doi.org/10.1016/j.ijthermalsci.2019.04.029.
[9] M. Longeon, A. Soupart, J.F. Fourmigué, A. Bruch, P. Marty, Experimental and numerical study of annular PCM storage in the presence of natural convection, Appl. Energy 112 (2013) 175–184, https://doi.org/10.1016/j.apenergy.2013.06.007.
[10] P.A. Bahrami, Natural melting within a spherical shell (No. A-90153), 1990.
[11] F.L. Tan, Constrained and unconstrained melting inside a sphere, Int. Commun. Heat Mass. Transf. 35 (2008) 466–475, https://doi.org/10.1016/j.icheatmasstransfer.2007.09.008.
[12] J.P. Bédécarrats, J. Castaing-Lasvignottes, F. Strub, J.P. Dumas, Study of a phase change energy storage using spherical capsules. Part I: experimental results, Energy Convers. Manag. 50 (2009) 2527–2536, https://doi.org/10.1016/j.enconman.2009.06.004.
[13] E. Borri, J.Y. Sze, A. Tafone, A. Romagnoli, Y. Li, G. Comodi, Experimental and numerical characterization of sub-zero phase change materials for cold thermal energy storage, Appl. Energy 275 (2020), 115131, https://doi.org/10.1016/j.apenergy.2020.115131.
[14] B. Weigand, Z. Lipnicki, Development of the contact layer and its role in the phase change process, Int. J. Heat Mass Transf. 93 (2016) 1082–1088, https://doi.org/10.1016/j.ijheatmasstransfer.2015.10.070.
[15] K. Merlin, D. Delaunay, J. Soto, L. Traonvouez, Heat transfer enhancement in latent heat thermal storage systems: comparative study of different solutions and thermal contact investigation between the exchanger and the PCM, Appl. Energy 166 (2016) 107–116, https://doi.org/10.1016/j.apenergy.2016.01.012.
[16] P. Giménez, A. Jové, C. Prieto, S. Fereres, Effect of an increased thermal contact resistance in a salt PCM-graphite foam composite TES system, Renew. Energy 106 (2017) 321–334, https://doi.org/10.1016/j.renene.2017.01.032.
[17] M. Thonon, G. Fraisse, L. Zalewski, M. Pailha, Analytical modelling of PCM supercooling including recalescence for complete and partial heating/cooling cycles, Appl. Therm. Eng. 190 (2021), 116751, https://doi.org/10.1016/j.applthermaleng.2021.116751.
[18] B. Feng, Y.H. Zhang, J. Tu, L.W. Fan, Z.T. Yu, Correlating the thermal contact resistance between metal/erythritol interfaces with surface roughness and contact pressure, Int. J. Heat Mass Transf. 176 (2021), 121407, https://doi.org/10.1016/j.ijheatmasstransfer.2021.121407.
[19] N. Calvet, X. Py, R. Olivès, J.P. Bédécarrats, J.P. Dumas, F. Jay, Enhanced performances of macro-encapsulated phase change materials (PCMs) by intensification of the internal effective thermal conductivity, Energy 55 (2013) 956–964, https://doi.org/10.1016/j.energy.2013.03.078.
[20] M. Díaz-Heras, J.F. Belmonte, J.A. Almendros-Ibáñez, Effective thermal conductivities in packed beds: review of correlations and its influence on system performance, Appl. Therm. Eng. 171 (2020), 115048, https://doi.org/10.1016/j.applthermaleng.2020.115048.
[21] Z. Liao, C. Xu, Y. Ren, F. Gao, X. Ju, X. Du, A novel effective thermal conductivity correlation of the PCM melting in spherical PCM encapsulation for the packed bed TES system, Appl. Therm. Eng. 135 (2018) 116–122, https://doi.org/10.1016/j.applthermaleng.2018.02.048.
[22] J.P. Bédécarrats, J. Castaing-Lasvignottes, F. Strub, J.P. Dumas, Study of a phase change energy storage using spherical capsules. Part II: numerical modelling, Energy Convers. Manag. 50 (2009) 2537–2546, https://doi.org/10.1016/j.enconman.2009.06.003.
[23] I. Sarbu, A. Dorca, Review on heat transfer analysis in thermal energy storage using latent heat storage systems and phase change materials, Int. J. Energy Res. 43 (2019) 29–64, https://doi.org/10.1002/er.4196.
[24] X. Yang, Q. Bai, Q. Zhang, W. Hu, L. Jin, J. Yan, Thermal and economic analysis of charging and discharging characteristics of composite phase change materials for cold storage, Appl. Energy 225 (2018) 585–599, https://doi.org/10.1016/j.apenergy.2018.05.063.
[25] H. Koizumi, Time and spatial heat transfer performance around an isothermally heated sphere placed in a uniform, downwardly directed flow (in relation to the enhancement of latent heat storage rate in a spherical capsule), Appl. Therm. Eng. 24 (2004) 2583–2600, https://doi.org/10.1016/j.applthermaleng.2004.03.011.
[26] S. Aziz, N.A.M. Amin, M.S. Abdul Majid, M. Belusko, F. Bruno, CFD simulation of a TES tank comprising a PCM encapsulated in sphere with heat transfer enhancement, Appl. Therm. Eng. 143 (2018) 1085–1092, https://doi.org/10.1016/j.applthermaleng.2018.08.013.
[27] R. Al-Shannaq, B. Young, M. Farid, Cold energy storage in a packed bed of novel graphite/PCM composite spheres, Energy 171 (2019) 296–305, https://doi.org/10.1016/j.energy.2019.01.024.
[28] J. Gasia, J.M. Maldonado, F. Galati, M. De Simone, L.F. Cabeza, Experimental evaluation of the use of fins and metal wool as heat transfer enhancement techniques in a latent heat thermal energy storage system, Energy Convers. Manag. 184 (2019) 530–538, https://doi.org/10.1016/j.enconman.2019.01.085.
[29] K. Nakaso, H. Teshima, A. Yoshimura, S. Nogami, Y. Hamada, J. Fukai, Extension of heat transfer area using carbon fiber cloths in latent heat thermal energy storage tanks, Chem. Eng. Process. Process Intensif. 47 (2008) 879–885, https://doi.org/10.1016/j.cep.2007.02.001.
[30] S. Feng, Y. Zhang, M. Shi, T. Wen, T.J. Lu, Unidirectional freezing of phase change materials saturated in open-cell metal foams, Appl. Therm. Eng. 88 (2015) 315–321, https://doi.org/10.1016/j.applthermaleng.2014.09.055.
[31] Verdonck E, Dreezen G. Thermal Conductivity Measurements of Conductive Epoxy Adhesives by MDSC®. n.d.
[32] N. Yüksel, The review of some commonly used methods and techniques to measure the thermal conductivity of insulation materials numan, in: A. Almusaed, A. Almssad (Eds.), Insul. Mater. Context Sustain., 2016, https://doi.org/10.5772/57353.
[33] F. Frusteri, V. Leonardi, S. Vasta, G. Restuccia, Thermal conductivity measurement of a PCM based storage system containing carbon fibers, Appl. Therm. Eng. 25 (2005) 1623–1633, https://doi.org/10.1016/j.applthermaleng.2004.10.007.
[34] Hukseflux thermal sensors. TPSYS02 thermal conductivity measurement, System. (2008), https://doi.org/10.1080/13645700310011215.
[35] A. Palacios, L. Cong, M.E. Navarro, Y. Ding, C. Barreneche, Thermal conductivity measurement techniques for characterizing thermal energy storage materials – a review, Renew. Sust. Energ. Rev. 108 (2019) 32–52, https://doi.org/10.1016/j.rser.2019.03.020.
[36] X.H. Yang, T.J. Lu, T. Kim, Temperature effects on the effective thermal conductivity of phase change materials with two distinctive phases, Int. Commun. Heat Mass. Transf. 38 (2011) 1344–1348, https://doi.org/10.1016/j.icheatmasstransfer.2011.08.021.
[37] C. Prieto, A. Lopez-Roman, N. Martínez, J.M. Morera, L.F. Cabeza, Improvement of phase change materials (PCM) used for solar process heat applications, Molecules 26 (2021) 1–13, https://doi.org/10.3390/molecules26051260.
[38] N.A.M. Amin, F. Bruno, M. Belusko, Effective thermal conductivity for melting in PCM encapsulated in a sphere, Appl. Energy 122 (2014) 280–287, https://doi.org/10.1016/j.apenergy.2014.01.073.
[39] N.H.S. Tay, F. Bruno, M. Belusko, Experimental validation of a CFD and an ε-NTU model for a large tube-in-tank PCM system, Int. J. Heat Mass Transf. 55 (2012) 5931–5940, https://doi.org/10.1016/j.ijheatmasstransfer.2012.06.004.
[40] R. Waser, F. Ghani, S. Maranda, T.S. O'Donovan, P. Schuetz, M. Zaglio, et al., Fast and experimentally validated model of a latent thermal energy storage device for system level simulations, Appl. Energy 231 (2018) 116–126, https://doi.org/10.1016/j.apenergy.2018.09.061.
[41] TESLAB@NTU. Thermal Energy Systems Lab n.d. https://www.thermalenergysystemslab.com/ (accessed September 19, 2021).

[42] B. Stroustrup, The C++ Programming Language, Second edition, Addison-Wesley, Reading, Mass., 1995 reprinted with corrections August, 1995. ©1991; 1995.
[43] Gbarivazhagan. 3d Heat conduction C code 2016.
[44] R. Turner, D. Eriksson, M. McCourt, J. Kiili, E. Laaksonen, Z. Xu, et al., Bayesian Optimization Is Superior to Random Search for Machine Learning Hyperparameter Tuning: Analysis of the Black-Box Optimization Challenge 2020, 2021.
[45] The scikit-optimize Contributors. scikit-optimize Documentation 2021.
[46] P.I. Frazier, A Tutorial on Bayesian Optimization, 2018, pp. 1–22.
[47] rmsolgi. geneticalgorithm 2020. https://github.com/rmsolgi/geneticalgorithm (accessed August 22, 2021).
[48] G. Van Rossum, F.L. Drake, Python 3 Reference Manual, CreateSpace, Scotts Valley, CA, 2009.
[49] I. Iriarte-Carretero, M.A. Gonzalez, F. Bresme, Thermal conductivity of ice polymorphs: a computational study, Phys. Chem. Chem. Phys. 20 (2018) 11028–11036, https://doi.org/10.1039/c8cp01272e.
[50] O. Andersson, A. Inaba, Thermal conductivity of crystalline and amorphous ices and its implications on amorphization and glassy water, Phys. Chem. Chem. Phys. 7 (2005) 1441–1449, https://doi.org/10.1039/b500373c.
[51] A.H. Harvey, Properties of ice and supercooled water, in: CRC Handb Chem Phys, 2019. https://tsapps.nist.gov/publication/get_pdf.cfm?pub_id=926353 (accessed August 30, 2021).
[52] Z. Lipnicki, T. Małolepszy, Analytical study of the solidification of a phase change material in an annular space, Energies 13 (2020), https://doi.org/10.3390/en13215561.
[53] N. Maeno, Air bubble formation in ice crystals, Econ. Stud. 63 (2) (1967) 1–86, 97-109.
[54] S.J. McClane, T.E. Hamilton, C.V. Burke, S.E. Raper, Functional consequences of adenovirus-mediated murine pancreatic gene transfer, Hum. Gene Ther. 8 (1997) 739–746, https://doi.org/10.1089/hum.1997.8.6-739.
[55] T. Yakhno, V. Yakhno, Two-phase water: structural evolution during freezing-thawing according to optical microscopy, arXiv preprint (2018) arXiv:1811.06768.
[56] W. Huang, Z. Li, X. Liu, H. Zhao, S. Guo, Q. Jia, Effective thermal conductivity of reservoir freshwater ice with attention to high temperature, Ann. Glaciol. 54 (2013) 189–195, https://doi.org/10.3189/2013AoG62A075.